Dynamics of a Giant Slow Landslide Along the Coast of the Aral Sea, Central Asia

Gokhan ASLAN[1], Marcello de Michele[1], Daniel Raucoules[2], François Renard[3], and Ziyadin Çakir[4]

[1]BRGM
[2]BRGM Service géologique national
[3]University of Oslo
[4]Istanbul Technical University

November 23, 2022

Abstract

We report here a slow-moving landslide revealed by Sentinel-1 interferometric time-series analysis. Located along the western coast of the Aral Sea, with a >80-km length and 4-km width, this is the world's largest active landslide complex reported so far with a constant velocity of 40 mm/yr. Systematic subsidence up to 5 mm/yr, is also observed along narrow strips of terraces that appear to result from rotations of fault-bounded blocks. The horizontal deformation does not correlate with the annual variations of the water level in the Aral Sea over the same period, indicating a long-term forcing of this landslide that might be caused by the long-term sea-level drop. The lateral spreadings involve the competent limestone beds lying horizontally on plastic clay- and evaporite-rich layers. We propose a conceptual model for the mechanism of landslides that appear to be controlled by the attitude of bedding, lithological sequence, hydrogeology, and low angle faults.

Hosted file

`aslan_etal_2021_aral_supporting-information_15_04_2021.docx` available at https://authorea.com/users/217762/articles/601877-dynamics-of-a-giant-slow-landslide-along-the-coast-of-the-aral-sea-central-asia

Posted on 23 Nov 2022 — CC-BY 4.0 — https://doi.org/10.1002/essoar.10507303.1 — This a preprint and has not been peer reviewed. Data may be preliminary.

Dynamics of a Giant Slow Landslide Along the Coast of the Aral Sea, Central Asia

G. Aslan[1,†], M. De Michele[1], D. Raucoules[1], F. Renard[2,3], Z. Cakir[4]

[1]Natural Risk Department, BRGM—French Geological Survey, 3 Claude-Guillemin 45060 Orléans, France

[2]Université Grenoble−Alpes, Université Savoie Mont Blanc, CNRS, IRD, IFSTTAR, ISTerre, Grenoble, France

[3]The Njord Centre, Department of Geosciences, University of Oslo, Oslo, Norway

[4]Department of Geological Engineering, Istanbul Technical University (ITU), Istanbul 34467, Turkey

†Corresponding author: Gökhan Aslan (g.aslan@brgm.fr)

Key Points:

- Sentinel-1 SAR data unravel the world's largest reported active lateral rock spreading complexes near the Aral Sea
- A >80 km long section of the west bank of Aral Sea is moving at an average rate of 4 cm/ yr over the period 2015-2020
- These landslides involve the lateral spreading and rotations of competent limestone beds overlying weak clays-rich layers
-

Abstract

We report here a slow-moving landslide revealed by Sentinel-1 interferometric time-series analysis. Located along the western coast of the Aral Sea, with a >80-km length and 4-km width, this is the world's largest active landslide complex reported so far with a constant velocity of 40 mm/yr. Systematic subsidence up to 5 mm/yr, is also observed along narrow strips of terraces that appear to result from rotations of fault-bounded blocks. The horizontal deformation does not correlate with the annual variations of the water level in the Aral Sea over the same period, indicating a long-term forcing of this landslide that might be caused by the long-term sea-level drop. The lateral spreadings involve the competent limestone beds lying horizontally on plastic clay- and evaporite-rich layers. We propose a conceptual model for the mechanism of landslides that appear to be controlled by the attitude of bedding, lithological sequence, hydrogeology, and low angle faults.

Plain Language Summary

Space-based measurements of slow ground motions of the Earth's surface provide a new tool to improve the understanding of various geophysical phenomena such as earthquakes, volcanoes, landslides, etc. with spatiotemporal aspects. We take advantage of recent advances in satellite-based radar interferometry techniques to measure the spatio-temporal evolution of the surface velocities of slow-moving landslide complexes along the western coast of the Aral Sea. We used three data sets comprising interferometric radar images obtained from different viewing geometries to monitor the lateral spreading motion over the study area from 2014 to 2020. We also compared the surface velocities obtained by the InSAR time series with the water-level height variations of the Aral Sea and find that the long-term forcing of this landslide might be caused by the long-term sea-level drop.

1 Introduction

Slow-moving landslides are a form of ground motion that occur in mechanically weak, clay-rich soil, and rock formations (Lacroix et al., 2020). Although, slow-moving landslides rarely claim lives (Mansour et al., 2011), they can pose a high risk to local infractructure and public safety. Slow-moving landslides creep at rates ranging from millimetres to several metres per year with almost constant slip rate (Palmer, 2017; Schulz et al., 2018). They play a major role in controlling the Earth surface processes in a variety of ways, from sediment transport, to hillslope denudation, and landscape erosion (Mackey & Roering, 2011; Schmidt & Montgomery, 1995; Simoni et al., 2013). However, constraining the mechanisms that control their movements is a challenging task because these events are variable both in time and space and are closely linked to the spatial and temporal stochastic nature of the environment, such as geology, geomorphology, vegetation, earthquakes and precipitation rate, among other parameters (van Asch et al., 2017; Hu et al., 2020). Thus, measuring the surface displacement field of landslides at high space and time resolution is essential to better constrain failure mechanism and define hazard and consequent risk senarios.

The Persistent Scatterer (PS) interferometry technique has allowed achieving significant results in monitoring and quantifying slow-moving landslides (Righini et al., 2012; Notti et al., 2010; Bovenga et al., 2012; Cigna et al., 2013; Tofani et al., 2013; Herrera et al., 2011; Carlà et al., 2019; Aslan et al., 2020; Lacroix et al., 2020). This technique has also proven its effectiveness for monitoring lateral rock spreading processes at different scales (Frodella et al., 2016; Mateos et al., 2018; Galve et al., 2017; Vicari et al., 2019). In the present study, we compute time series of the ground deformation fields acquired by satellite imaging over two study areas on the west coast of the Aral Sea over the eastern edge of the Ustyurt Plateau (Fig. 1). Results report the slow horizontal and vertical moving kinematics and dynamics of a gigantic, 80 km long, lateral spreading of rock mass over a six-year period.

2 Study area and background

The Ustyurt plateau, is located between the Mangyshlak Peninsula and Kara-Bogaz-Gol lagoon of the Caspian Sea to the west, and the Aral Sea and Amudarya Delta to the east (Fig. 1a). The plateau stretches > 1500 km from north to south. Brittle Sarmatian limestones (Upper Miocene) overlying Miocene and Paleogene marls, chalks, claystone, and sand control its topography (Garetsky, 1972). Its edges are separated from adjacent territories by very steep scarps, also called tchink, with vertical rock exposures reaching up to 250 m high on the western coast of the Aral Sea. The tchinks are the most striking topographical objects in the whole region that extends hundreds of kilometers to the west until the shallow gulf of the Caspian Sea (Fig. 1a). The coastal geomorphic response to sea-level and climate changes, particularly along the boundaries of the Ustyurt Plateau, remains enigmatic. However, it is widely accepted that sea transgression in the late Pleistocene (40–25 ka BP) inundated vast portions of the low-lying semi-desert of western Kazakhstan and Uzbekistan (Pánek et al., 2016). Cliff cuts during these highstands generated the prominent over-steepened escarpments that presently surrounds the Ustyurt Plateau. This region is affected by giant landslides (>10^8m^3) in a form of complex lateral rock spreadings and the present day cinematic of these landslides is unknown.

These landslides share characteristics of lateral rock spreads along nearly horizontal basal failure planes involving brittle limestones overlying weak and plastic claystone (Pánek et al., 2016). Although similar landforms have been observed along the present-day coastline of the Caspian Sea and Aral Sea, it remains unclear whether some of these landslides are still active today and whether the movement is slow or catastrophic.

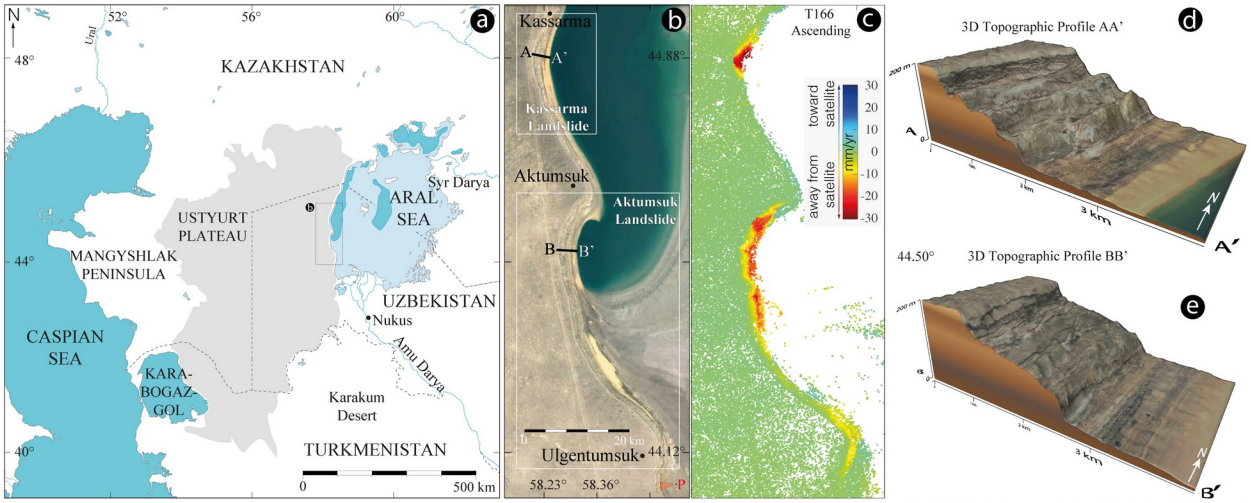

Figure 1. Map of the Aral Sea region showing the geographic position of **(a)** the Ustyurt Plateau, **(b)** the study areas along the eastern cliff of the plateau near the western coast of the Aral Sea, mean line−of−sight (LOS) velocity fields over the study areas obtained from the descending orbit (T166) and three-dimensional topographic cross-sections for profiles AA' and, **(d)** BB' **(e)**. The line AA' in **(b)** indicates the location of the cross-section plotted in Fig. 4. The point P in the bottom right in **(b)** indicates the viewpoint and perspective of the photo in Fig. S1.

The two selected areas are located between the eastern cliff of the Ustyurt plateau and the western coast of the Aral Sea and extend >80 km length in a north-south direction with a landward expansion of 0.5-1.5 km on the coastal ledges to 2.5-4.0 km on the concave sections (Fig. 1b). The areas under consideration are bounded on their east side by a strip of dry land and a beach, at the foot of which fragments of ancient Aral Sea terraces are located, and on their west side by the sharp upper edge of the Ustyurt plateau. The study area contains the deepest coastal bottom of the Aral Sea (40 m below sea level near Kassarma, Fig. 1b). The slope of the cliff adjoining from the rear to low sea terraces is characterized by straight, and sometimes concave

profiles. The base of the cliff is covered by colluvial and aluvial sediments deposited during the 20th century (Bronguleyev & Rozanov, 1978). The foot of the cliff is covered with aeolian sands that form coastal dunes and tongues that move along the slope of the cliff under the effect of wind, blocking the mouths of ravines (Veynbergs, 1972). The coastal zone along the concave sections is mostly covered by Upper Quaternary sediments, mainly clayey fine-grained dry sands and interlayered pebble-beds (Lymarev, 1967). The surface of the narrow strips of terraces consists of a regular alternation of several (2-4) parallel Sarmatian limestone blocks and depressions (Fig. 1d,1e and Fig. S1). Subvertical cliffs, also called ramparts, are composed of red-colored Oligocene-Miocene clays and marls, which also contain scattered pack of gypsum-rich layers covered with crushed to large blocks and partially washed away by the armor of Sarmatian white shell limestones and marls (Bronguleyev & Rozanov, 1978).

Rock or block spreading is defined as the lateral expansion of fractured rock masses occurring along shear or tensile discontinuities (Cruden & Varnes, 1996; Bobrowsky, 2013). Such processes may develop on nearly horizontal slopes where brittle rocks overly weak and more ductile layers (Bois et al., 2018) and several conceptual models have been proposed (Fig. S2). In addition to kinematic and geological predisposing factors, erosion and tectonics, or their combination in space and time, are the main driving factors for lateral spreading, resulting in over-steepened slopes that are kinematically unconstrained at their toe and that can move freely in a lateral direction (Alfaro et al., 2019) (Fig. S2b, c). Various studies have reported a large variety of such lateral rock spreading movements. Striking examples come from Czech Republic, where a weak marl and shale substrate deforms under the weight of sandstone blocks (Zaruba & Mencl, 2014). In the Italian Apennines, lateral spreading occurs due to widespread overlapping of volcanic or sedimentary stiff rock masses on more ductile clay shales layer (e.g., Canuti et al., 1990; Picarelli & Russo, 2004; Bozzano et al., 2013). Lateral spreading may also occur by multiple retrogressive sliding failures where a number of instabilities exploit a single weak horizon (Hungr et al., 2014) (Fig. S2d). Spectacular examples of lateral spread in South Saskatchewan, Canada are caused by multiple retrogressive compound sliding in glacio-lacustrine clay overlying Cretaceous shale (Haug et al., 1977; Mollard & Janes, 1984). Another spreading mechanism may be involved when rigid blocks of brittle rocks are underlain by soluble evaporitic formations where water percolation and hydrogeologic conditions will play critical roles in interstratal evaporite dissolution (Gutierrez et al., 2012) (Fig. S2e).

3 InSAR Data and Methodology

We used data from the European Space Agency Sentinel-1 SAR constellation, which is composed of two satellites that were launched in April 2014 (S1A) and April 2016 (S1B) and equipped with C-band SAR sensors. The Sentinel-1 operation in Terrain Observation with Progressive Scan (TOPS) mode represents an important advantage compared to other sensors' modes as it provides wide area coverage and a short revisit time of up to 6-days over Europe and 12-days globally. Here, we processed SAR datasets acquired on three overlapping tracks in descending (T166) and ascending (T13, T86) orbits, consisting respectively of 74, 93 and 110 images over the period of 2015-2020 (Fig. S3). We employed an individual set of interferograms for each track with a sufficiently high phase coherence pattern over the study area. The region examined here is arid with fairly flat topography and with almost no vegetation. These conditions provide a favorable image coherency for interferometric SAR processing.

We computed all interferograms using the open-source software GMTSAR (Sandwell et al., 2011) based on a single reference network for persistant scatterer interferometry analysis. The choice of the reference images is made on the basis of having the most optimal spatial and temporal baselines for all the pairs of interegrams (Fig. S3). To compute the simulation of topographic phase in the interferograms, we used the Shuttle Radar Topography Mission 3-arcsecond digital elevation model (Farr et al., 2007). We processed the single master stacks of interferograms using the StaMPS software package (Hooper, 2008; Hooper et al., 2012), which

allows the identification of PS points, using both amplitude and phase information. In a first step, the initial PS points are selected based on their noise characteristics, using the amplitude dispersion criterion defined by $D_{amp}=(\sigma_{Amp}/m_{Amp})$, where σ_{Amp} and m_{Amp} are the standard deviation and mean of the amplitude in time, respectively (Ferretti et al., 2001). We selected a threshold value of $D_{amp}=0.27$ that minimizes the random amplitude variability and eliminates highly decorrelated pixels in some areas covered with vegetation, agricultural fields, or snow. After the selection of stable PS targets based on amplitude analysis, the PS probability is refined by phase analysis in a series of iterations. This process allows the detection of stable pixels even with low amplitude. Once the final selection of PSs has been done, the residual topographic component can be removed. Then, phase unwrapping is performed both spatially and temporally. This analysis enables retrieval of the average Line-Of-Sight (LOS) surface deformation rate maps. To remove atmospheric effects from interferograms, we used the freely available Toolbox for Reducing Atmospheric InSAR Noise (Bekaert et al., 2015). This toolbox uses ERA-Interim (ERA-I, European Center for Medium-Range Weather Forecast) numerical weather model datasets (Dee et al., 2011). Finally, we decomposed the mean PS-InSAR LOS velocity fields into vertical and east-west horizontal components using the formulation described by Samieie-Esfahany et al. (2009). We neglected here the motion along the north−south direction, which a reasonable assumption for an eastward slope motion.

4 Results

Time series analysis of 277 Sentinel IW SAR images on the three tracks reveals the spatio-temporal evolution of the landslide complex over both study areas (Figs. 1c, 2 and 3). The mean line-of-sight (LOS) and vertical and horizontal maps show that the landmass is sliding mainly horizontally toward the Aral Sea at a LOS velocity of up to 4 cm/year. The vertical velocity maps displayed in Figs. 2e and 3e show also relatively higher rates of vertical motions (yellow to red areas) localized along narrow stripes of terraces formed by secondary slip planes. The narrow strip between the shoreline and PS points (in white in Figs. 2 and 3) consists of a sandy layer and is lacking scatter points due to temporal decorrelation. The landslide complexes cover surface areas of approximately 30 km^2 and 115 km^2 for the Kassarma and Aktumsuk landslide zones, respectively. While the Kassarma landslide exhibits one main sliding zone in an amphitheater-shaped bounded by stable the Ustyurt Plateau (Fig. 2), the Aktumsuk landslide complex shows several sliding zones with varying velocities and forms (Fig. 3).

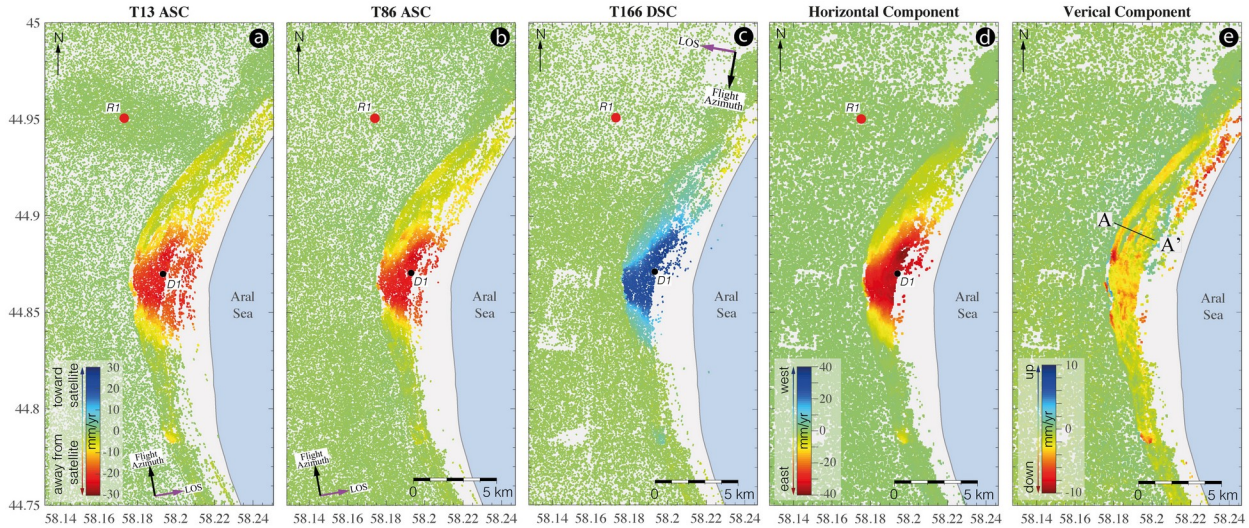

Figure 2: InSAR mean line-of-sight along the three tracks (a-c), east-west horizontal (d) and (e) vertical velocity maps of the Kassarma Landslide located between Kassarma and Aktumsuk capes, for the period 2015–2020 from permanent scatterer interferometric synthetic aperture radar time series. In a-c) negative velocities (cold colors) represent the motion of the ground toward the satellite and positive velocities (warm colors) represent motion away from the satellite. The mean velocity value of the PS-InSAR points within the solid black point (D1) is used to illustrate the temporal evolution of the landslide (Fig. 4) deformation with respect to a reference point (red point R1) considered as a stable area on the plateau. The red point (R1) also shows the location to which all InSAR velocities are referenced before decomposition of LOS maps into horizontal and vertical components.

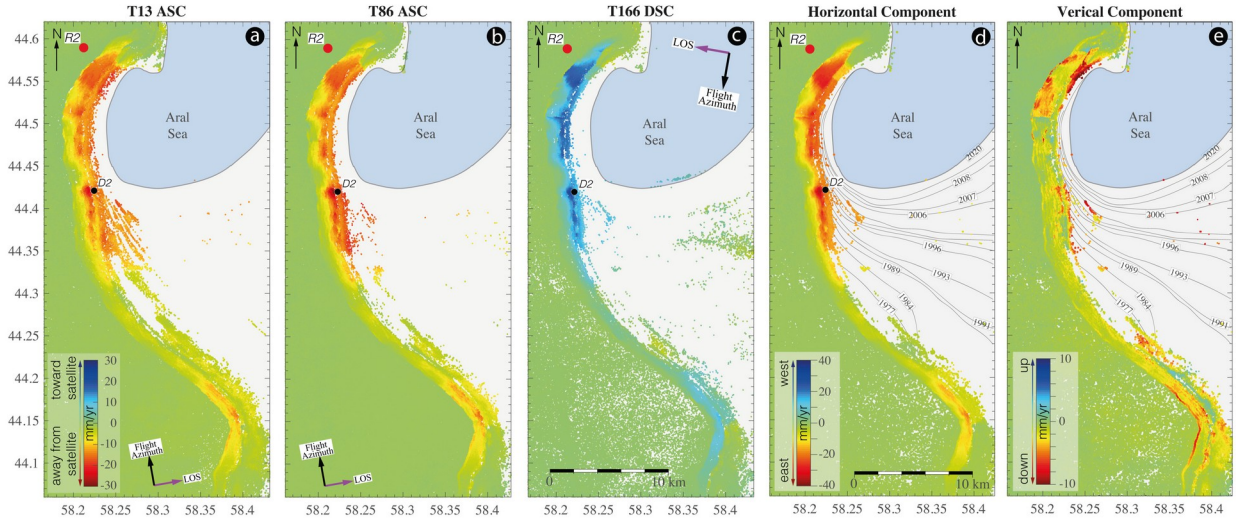

Figure 3: Mean line−of−sight (LOS) velocity fields of the Aktumsuk Landslide located between Aktumsuk and Ulgentumsuk capes and deformation decomposition into 2D displacement rates for the period 2015-2020. **(a)-(e)** as labeled in Fig. 2. R2 and D2 are reference points similar to that in Fig. 2. Contours of the former shorelines in (d) and (e) are taken from Ginzburg et al., (2010).

Analysed time series of displacement are represented by the average accumulated displacement of the points in one selected unstable area (points D1 and D2 in Figs. 2 and 3) with respect to reference PS points (points R1 and R2) for each track. Landslide time series show an overall linear trend of displacement with time (Fig. S4) for both selected areas. The water level of the Aral Sea obtained from TOPEX/POSEIDON and Jason series altimetry data shows also a linear trend, with seasonal variations, with a decrease of 2.5 m over the same period 2015-2020. This is no clear correlation between the seasonal variations of the Aral Sea and the landslide motion. The maximum cumulative deformation in line-of-sight (LOS) direction in both study areas is around 20 cm during the six year long observation period. The region is one of the driest deserts in the world, with a precipitation rate less than 100 mm per year (Amirov et al., 2015). Such a small quantity of precipitation is the only contributor to the hydrological budget in this area.

The computed vertical and horizontal components of the surface displacement fields across the Kassarma study area (Fig. 4a and 4b) located between Kassarma and Aktumsuk capes (section A-A' in Fig. 1b and 1d) are compared with the geological and geomorphological cross-section of the landslide in the Figure 4. The observed rates of horizontal and vertical displacements and their spatial variations across the landslide provide evidence of the landslide failure mechanism where blocks of limestones over the weak clay layer are detached from the Ustyurt plateau and move ovewhelmingly horizontally toward the Aral Sea with insignificant component of vertical motion. The pattern of vertical motion across the landslide is remarkably systematic and

indicates backward rotations of the individual blocks (Fig. 4b and 4c). This implies that the near horizontal motion we observe is not a gravitational rock spreading but, accommodated by low angle listric faults that sole into a near horizontal detachment as observed by the Kara-Bogaz-Gol lagoon of the Caspian Sea.

5 Discussion and Conclusions

We report the discovery of an active, gigantic, lateral spreading failure along the western coast of the Aral Sea. Previous studies in this area have focused on sea terraces and the beach strips of the coast with little discussions on the mechanism and kinematics of the spreadings. The morphological signature of the spreading mechanism has been studied by Lymarev, (1967) and Bronguleyev & Rozanov, (1978), based on extensive geological field data. Here, we fully constrain and resolve the present day kinematics of this gigantic lateral spreading along the western coast of the Aral Sea.

The Kassama landslide complex exhibits a very peculiar characteristics of a multiple rotational landslides. The proposed mechanism consists of the break-down of blocks of Sarmatian limestones that lose adhesion to the main limestone layer covering the Ustyurt plateau. This limestone overlies a weak clay layer. The absolute altitude of the limestone blocks decreases in the direction from the cliff to the coast of the Aral Sea in a very regular fashion that resulted in a stair-step topography (Fig. 4a). This systematic decrease in the absolute altitude of the blocks across the landslide implies their manifold development of the same mode of movement in time. Such type of rock rotational slides usually occurs in very weak or highly jointed rock masses often under the surcharge of a stronger cap rock (Hungr et al., 2014).

The vertical and horizontal components of the surface displacement fields across the geological and geomorphological section of the Kassarma Landslide show very clearly the sliding mechanism of the landslide complex (Fig. 4a, 4b and 4c). The observed sharp discontinuities across the both velocity profiles in Fig. 4a and 4b coincide with the successive and regularly-spaced steep scarps that we interpret as potential fault planes where rotational sliding occurs. The horizontal deformation pattern in the Fig. 4a shows that each block experiences horizontal displacement with varying velocities ranging from 5 mm/yr at the head scarp to 30 mm/yr at the toe of the landslide. Horizontal velocity increases toward the free-face of the slope; in other words the landslide's toe moves eastward faster than the rest of landslide (Fig. 4d), resulting in tensional forces and hence extensional slope-parallel cracks. This spatial variation in the horizontal displacement rates points again to the rotational mechanism. Another characteristic surface feature in the depletion zone of rotational landslides are sag ponds, small water bodies filling depressions where landslide movement has impounded the drainage (Fig. S5). Several well defined sag ponds are also identified on satellite optical images developed on back-tilted landslide surfaces or inter-hummock depressions (Fig. S5). The vertical deformation pattern in the Fig. 4b is characterized by a prominent main scarp and back-tilted blocks at top with limited internal deformation. Each block rotates backward towards the cliff line, as the ground moves eastward on a curved sliding surface. Such a rotational motion results in relative sinking between the blocks (Fig. 4b).

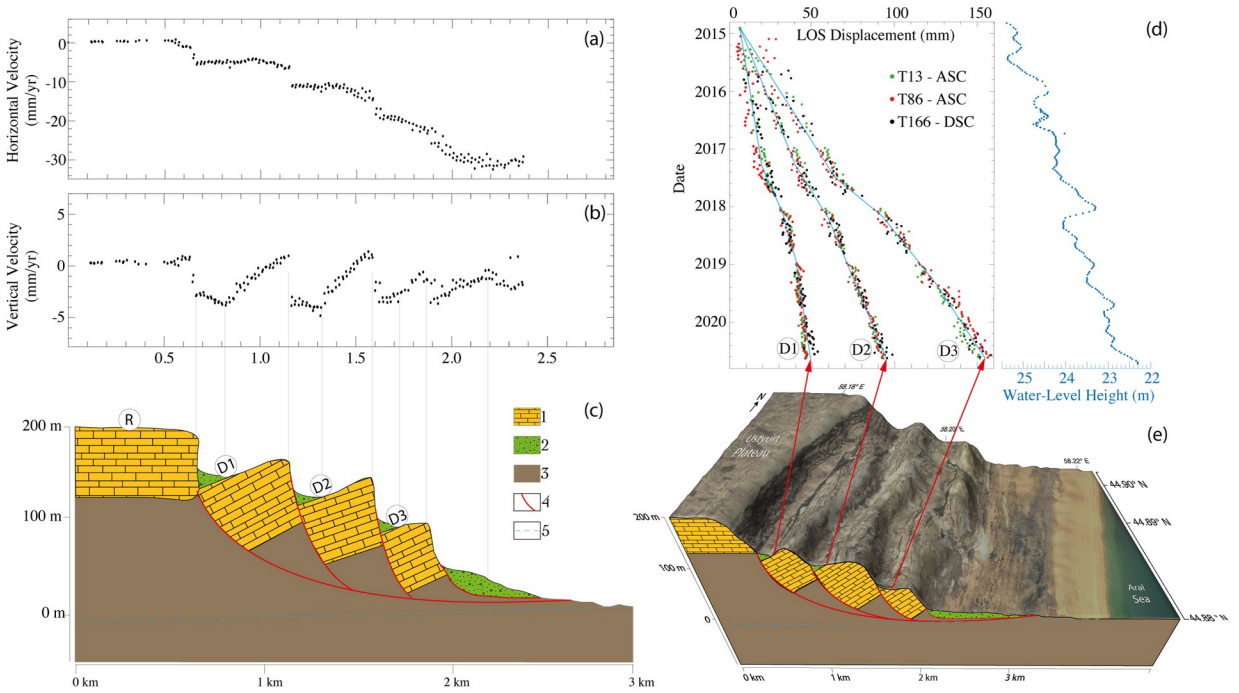

Figure 4: The horizontal **(a)** and vertical **(b)** velocities along the AA' profile are displayed together with the schematic geological and geomorphological section of the landslide **(c). (d)** Time series of Line-of-Sight (LOS) direction estimated from each track at three specific locations (D1, D2 and D3 in (c)) of the each headblock with respect to a reference point R considered as a stable area on the plateau together with the water level height variations of the Aral Sea. **(e)** Three-dimensional rendering of rotational rock slide morphology looking from the south of the Profile AA' in Fig.1d. Collapsed limestone blocks are packed in Paleocene clays sliding towards the Aral Sea. 1 – limestones and marls; 2 – deposits of the beach, young terraces; 3 – clay; 4 – interpreted fault plane; 5 – Aral Sea level.

The toe areas of the hummocky slopes are apparently truncated by the wave-cut erosion of the Aral Sea. In addition, there are also giant individual landslides run out over 4 km along the eastern cliff of the Ustyurt plateau and some had their toes subsequently trimmed by wave erosion by the Aral Sea. The occurrence of these ancient landslides is predetermined by the active linear subsidence of the West Aral Basin related to an isostatic process (Aseyev et al., 1974). Data from our three independent sets of Sentinel-1A/B imagery indicate that these mega landslides were inactive over the period 2015-2020.

The lack of correlation between the deformation time-series obtained from all tracks and the annual variations of the water level in the South Aral Sea (Fig. S4) indicate that the absence of short-term interactions between these two. However, we suggest that the long-term, human induced, decrease of the water in the Aral Sea might have an influence on the landslide. Considering the existence of the gypsum-bearing layers in the soil profile over the deforming areas, a lowering of the Aral Sea water level (2.5 m in total during the observation period of 6 years) may enhance dissolution phenomena taking place in the zone near the decollement plane as salt layers expose to the underground fresh water. Such a reactivation of hidden karstic salt layers triggered sinkholes, subsidence and several hectometric landslides along the Dead Sea coasts (Closson & Karaki, 2009). However, more information on the hydro-geological structure and deformation mechanism of the landslide are needed to further validate this mechanism. On the other hand, most rotational rock slides show self-stabilizing characteristics as the gravitational driving forces diminish with increasing displacement (Hungr et al., 2014).

Therefore, they tend to move at slow or moderate velocities as the weak rock mass fails in a ductile as also can be seen in this study (Fig. S4) (Hungr and Evans, 2004).

Our study reveals possibly the largest active lateral rock spreading following rotational sliding on the planet. Altogether, multiple lines of morphological evidence and InSAR data demonstrate that the failure mechanism can be best described as lateral spreading on a low angle detachment with minor backward rotations on fault bounded blocks. If the seasonal fluctuations of the Aral Sea level do not correlate directly with the displacement rate of the landslide (Fig. S4), the long term decrease of the water level in this sea could represent a triggering and driving mechanism of this landslide, which would make it the largerst human-induced landslide on the planet. A future study that would use longer time series (i.e. ERS/ENVISAT) would help answering the links between the water level in the Aral Sea and the kinematics of the giant landslide discovered in the present study. Further analysis need to be performed in order to investigate its dynamics, mechanics and future evolution. Studies of the relationship between the kinematics of lateral rock spreading, hydrological forces, and the local stratigraphy along the eastern cliff of the Ustyurt plateau would benefit of multidisciplinary approaches: the combiniation of multi band InSAR (X-band, C band) with field investigation (ground-based SAR interferometry) as well as analog and numerical models in order to better assess the kinematic behavior of this phenomenon.

Acknowledgments

The raw interferometric products used in this study are freely distributed to the public via the European Space Agency within the framework of the Copernicus Sentinel-1 mission (https://scihub.copernicus.eu/). Processing of Sentinel 1A/B images is performed at TUBITAK ULAKBIM (The Turkish Academic Network and Information Centre), High Performance, and Grid Computing Center (TRUBA resources). TOPEX/POSEIDON and Jason series altimetry data provided by the USDA Global Reservoir and Lake Elevation Database, (https://ipad.fas.usda.gov/cropexplorer/global_reservoir). We thank David and Sue Richardson for providing the landslide photos used in this study (Fig. S1) taken durin the field investigation and Pascal Lacroix and Séverine Bernardie for providing feedback on an early version of this manuscript.

References

Alfaro, P., Delgado, J., Esposito, C., Tortosa, F. G., Marmoni, G. M., & Martino, S. (2019). Time-dependent modelling of a mountain front retreat due to a fold-to-fault controlled lateral spreading. *Tectonophysics*, 773, 228233. doi: 10.1016/j.tecto.2019.228233.

Amirov, S. S., Yagodin, V. N., & Betts, A. (2015). Mapping ancient hunting installations on the Ustyurt Plateau, Uzbekistan and Kazakhstan: New results from Remote Sensing Imagery. *Paléorient*, 199-219.

Aseyev, A.A., Banguleev, V.V., Muratov, V.M., et Pshenin, G.N. (1974). Processus exogènes et réaction de la croûte terrestre. *Géomorphologie*, (1), 3-14.

Aslan, G., Foumelis, M., Raucoules, D., De Michele, M., Bernardie, S., & Cakir, Z. (2020). Landslide Mapping and Monitoring Using Persistent Scatterer Interferometry (PSI) Technique in the French Alps. *Remote Sensing*, 12(8), 1305. doi: 10.3390/rs12081305

Bekaert, D. P. S., Walters, R. J., Wright, T. J., Hooper, A. J., & Parker, D. J. (2015). Statistical comparison of InSAR tropospheric correction techniques. *Remote Sensing of Environment*, 170, 40-47.

Bobrowsky, P. T. (Ed.). (2013). Encyclopedia of natural hazards (Vol. 1135). Dordrecht: Springer.

Bois, T., Zerathe, S., Lebourg, T., & Tric, E. (2018). Analysis of lateral rock spreading process initiation with a numerical modelling approach. *Terra Nova*, 30(5), 369-379. doi: 10.1111/ter.12352.

Bovenga, F., Wasowski, J., Nitti, D. O., Nutricato, R., & Chiaradia, M. T. (2012). Using COSMO/SkyMed X-band and ENVISAT C-band SAR interferometry for landslides analysis. *Remote Sensing of Environment*, 119, 272-285. doi: 10.1016/j.rse.2011.12.013.

Bozzano, F., Bretschneider, A., Esposito, C., Martino, S., Prestininzi, A., & Mugnozza, G. S. (2013). Lateral spreading processes in mountain ranges: Insights from an analogue modelling experiment. *Tectonophysics*, 605, 88-95. doi: 10.1016/j.tecto.2013.05.006.

Bronguleev, V., Pshenin., G. N. & Rozanov, L. L. (1978). O Mekhanizme Formirovaniya Rel'efa Vostochnogo Chinka Plato Ustyurt, *Geomorfologija* (Moskow), 2, 52-60.

Canuti, P., Casagli, N., Garzonio, C. A., & Vannocci, P. (1990). Lateral spreads and landslide hazards to the Northern Apennine. The example of Mt. Fumaiolo (Emilia Romagna) and Chiusi della Verna (Tuscany). In *International congress international association of engineering geology*, 6 (pp. 1525-1533).

Carlà, T., Intrieri, E., Raspini, F., Bardi, F., Farina, P., Ferretti, A., & Casagli, N. (2019). Perspectives on the prediction of catastrophic slope failures from satellite InSAR. *Scientific Reports*, 9(1), 1-9. doi: 10.1038/s41598-019-50792-y.

Cigna, F., Bianchini, S., & Casagli, N. (2013). How to assess landslide activity and intensity with Persistent Scatterer Interferometry (PSI): the PSI-based matrix approach. *Landslides*, 10(3), 267-283. doi: 10.1007/s10346-012-0335-7.

Closson, D., & Abou Karaki, N. (2009). Human-induced geological hazards along the Dead Sea coast. *Environmental Geology*, 58(2), 371-380. doi: 10.1007/s00254-008-1400-3.

Cruden, D. M., & Varnes, D. J. (1996). Landslides: investigation and mitigation. Chapter 3-Landslide types and processes. Transportation research board special report, 247, 36-75.

Dee, D. P., Uppala, S. M., Simmons, A. J., Berrisford, P., Poli, P., Kobayashi, S., & Vitart, F. (2011). The ERA−Interim reanalysis: Configuration and performance of the data assimilation system. *Quarterly Journal of the royal meteorological society,* 137(656), 553-597. doi: 10.1002/qj.828.

Farr, T. G., Rosen, P. A., Caro, E., Crippen, R., Duren, R., Hensley, S., & Alsdorf, D. (2007). The shuttle radar topography mission. *Reviews of geophysics*, 45(2). doi: 10.1029/2005RG000183.

Ferretti, A., Prati, C., & Rocca, F. (2001). Permanent scatterers in SAR interferometry. *IEEE Transactions on geoscience and remote sensing*, 39(1), 8-20. doi: 10.1109/36.898661.

Frodella, W., Ciampalini, A., Gigli, G., Lombardi, L., Raspini, F., Nocentini, M., & Casagli, N. (2016). Synergic use of satellite and ground based remote sensing methods for monitoring the San Leo rock cliff (Italy). *Geomorphology*, 264, 80-94. doi: 10.1016/j.geomorph.2016.04.008.

Gutiérrez, F., Linares, R., Roqué, C., Zarroca, M., Rosell, J., Galve, J. P., & Carbonel, D. (2012). Investigating gravitational grabens related to lateral spreading and evaporite dissolution subsidence by means of detailed mapping, trenching, and electrical resistivity tomography (Spanish Pyrenees). *Lithosphere*, 4(4), 331-353. doi: 10.1130/L202.1.

Galve, J. P., Pérez-Peña, J. V., Azañón, J. M., Closson, D., Caló, F., Reyes-Carmona, C., & Bally, P. (2017). Evaluation of the SBAS InSAR service of the European space Agency's Geohazard Exploitation Platform (GEP). *Remote Sensing*, 9(12), 1291. doi: 10.3390/rs9121291.

Garetsky, R. G. (1972). Tektonika molodykh platform Evrazii.

Ginzburg, A. I., Kostianoy, A. G., Sheremet, N. A., & Kravtsova, V. I. (2010). Satellite monitoring of the Aral Sea region. In *The Aral Sea Environment* (pp. 147-179). Springer, Berlin, Heidelberg.

Haug, M. D., Sauer, E. K., & Fredlund, D. G. (1977). Retrogressive slope failures at Beaver Creek, south of Saskatoon, Saskatchewan, Canada. *Canadian Geotechnical Journal*, 14(3), 288-301. doi: 10.1139/t77-035.

Herrera, G., Notti, D., García-Davalillo, J. C., Mora, O., Cooksley, G., Sánchez, M., & Crosetto, M. (2011). Analysis with C-and X-band satellite SAR data of the Portalet landslide area. *Landslides*, 8(2), 195-206. doi: 10.1007/s10346-010-0239-3.

Hooper, A. (2008). A multi−temporal InSAR method incorporating both persistent scatterer and small baseline approaches. *Geophysical Research Letters*, 35(16). doi: 10.1029/2008GL034654.

Hooper, A., Bekaert, D., Spaans, K., & Arıkan, M. (2012). Recent advances in SAR interferometry time series analysis for measuring crustal deformation. *Tectonophysics*, 514, 1-13. doi: 10.1016/j.tecto.2011.10.013.

Hu, X., Bürgmann, R., Schulz, W. H., & Fielding, E. J. (2020). Four-dimensional surface motions of the Slumgullion landslide and quantification of hydrometeorological forcing. *Nature Communications,* 11(1), 1-9. doi: 10.1038/s41467-020-16617-7.

Hungr, O., & Evans, S. G. (2004). The occurrence and classification of massive rock slope failure. *Felsbau*, 22(2), 16-23.

Hungr, O., Leroueil, S., & Picarelli, L. (2014). The Varnes classification of landslide types, an update. *Landslides*, 11(2), 167-194.

Lacroix, P., Handwerger, A. L., & Bièvre, G. (2020). Life and death of slow-moving landslides. *Nature Reviews Earth & Environment*, 1(8), 404-419. doi: 10.1038/s43017-020-0072-8

Lymarev, V. I. (1967). Berega Aral'skogo morâ, vnutrennego vodoema aridnoj zony. Nauka.

Mackey, B. H., & Roering, J. J. (2011). Sediment yield, spatial characteristics, and the long-term evolution of active earthflows determined from airborne LiDAR and historical aerial photographs, Eel River, California. *Geological Society of America Bulletin*, 123(7-8), 1560–1576. doi: 10.1130/B30306.1.

Mansour, M. F., Morgenstern, N. R., & Martin, C. D. (2011). Expected damage from displacement of slow-moving slides. *Landslides*, 8(1), 117-131. doi:10.1007/s10346-010-0227-7.

Mateos, R. M., Ezquerro, P., Azañón, J. M., Gelabert, B., Herrera, G., Fernández-Merodo, J. A., & Béjar-Pizarro, M. (2018). Coastal lateral spreading in the world heritage site of the Tramuntana Range (Majorca, Spain). The use of PSInSAR monitoring to identify vulnerability. *Landslides*, 15(4), 797-809. doi: 10.1007/s10346-018-0949-5.

Mollard, J. D., & Janes, J. R. (1984). Airphoto interpretation and the Canadian landscape. Energy, Mines, and Resources Canada.

Notti, D., Davalillo, J. C., Herrera, G., & Mora, O. (2010). Assessment of the performance of X-band satellite radar data for landslide mapping and monitoring: Upper Tena Valley case study. *Natural Hazards and Earth System Sciences*, 10(9), 1865. doi:10.5194/nhess-10-1865-2010.

Palmer, J. (2017). Creeping earth could hold secret to deadly landslides. *Nature News*, 548(7668), 384. doi: 10.1038/548384a.

Pánek, T., Korup, O., Minár, J., & Hradecký, J. (2016). Giant landslides and highstands of the Caspian Sea. *Geology*, 44(11), 939-942. doi: 10.1130/G38259.1.

Picarelli, L., & Russo, C. (2004). Remarks on the mechanics of slow active landslides and the interaction with man-made works. In *Landslides: evaluation and stabilization* (pp. 1141-1176), Balkema Publishers, Leiden.

Righini, G., Pancioli, V., & Casagli, N. (2012). Updating landslide inventory maps using Persistent Scatterer Interferometry (PSI). *International Journal of Remote Sensing*, 33(7), 2068-2096. doi: 10.1080/01431161.2011.605087.

Samieie-Esfahany, S., Hanssen, R., van Thienen-Visser, K., & Muntendam-Bos, A. (2009). On the effect of horizontal deformation on InSAR subsidence estimates. In Proceedings of the Fringe 2009 Workshop, Frascati, Italy (Vol. 30).

Sandwell, D., Mellors, R., Tong, X., Wei, M., & Wessel, P. (2011). Open radar interferometry software for mapping surface deformation. *Eos, Transactions American Geophysical Union*, 92(28), 234-234. doi: 10.1029/2011EO280002.

Schmidt, K. M., & Montgomery, D. R. (1995). Limits to relief. *Science*, 270(5236), 617–620. doi: 10.1126/science.270.5236.617.

Schulz, W. H., Smith, J. B., Wang, G., Jiang, Y., & Roering, J. J. (2018). Clayey landslide initiation and acceleration strongly modulated by soil swelling. *Geophysical Research Letters,* 45(4), 1888-1896. doi: 10.1002/2017GL076807.

Simoni, A., Ponza, A., Picotti, V., Berti, M., & Dinelli, E. (2013). Earthflow sediment production and Holocene sediment record in a large Apennine catchment. *Geomorphology*, 188, 42–53. doi: 10.1016/j.geomorph.2012.12.006.

Tofani, V., Raspini, F., Catani, F. & Casagli, N. (2013). Perisistent Scatterer Interferometry (PSI) technique for landslide characterization and monitoring. *Remote Sensing*, 5(3), 1045-1065. doi: 10.3390/rs5031045.

van Asch, T. W., Malet, J. P., van Beek, L. P., & Amitrano, D. (2007). Techniques, issues and advances in numerical modelling of landslide hazard. *Bulletin de la Société Géologique de France*, 178(2), 65-88. doi: 10.2113/gssgfbull.178.2.65.

Veynbergs I. G., Ul'st V.G., Roze V.K. O. (1972) drevnikh beregovykh liniyakh i kolebaniyakh urovnya Aral'skogo morya. Issues of *Quaternary Geology*. Riga, 6, Is. 6, pp. 3–11. (In Russian).

Vicari, A., Famiglietti, N. A., Colangelo, G., & Cecere, G. (2019). A comparison of multi temporal interferometry techniques for landslide susceptibility assessment in urban area: an example on stigliano (MT), a town of Southern of Italy. *Geomatics, Natural Hazards and Risk*, 10(1), 836-852. doi: 10.1080/19475705.2018.1549113.

Zaruba, Q., & Mencl, V. (2014). Landslides and their control. Elsevier.